The formation, transport properties and microstructure of 45° [001] grain boundaries induced by epitaxy modification in YBa₂Cu₃O₇₋ₓ thin films

The formation, transport properties and microstructure of 45° [001] grain boundaries induced by epitaxy modification in $YBa_2Cu_3O_{7-x}$ thin films

B.V. Vuchic [a], K.L. Merkle [a,*], P.M. Baldo [a], K.A. Dean [b], D.B. Buchholz [b], R.P.H. Chang [b], H. Zhang [b], L.D. Marks [b]

[a] *Materials Science Division, Argonne National Laboratory, Argonne, IL 60439, USA*
[b] *Materials Science and Engineering Department, Northwestern University, Evanston, IL 60208, USA*

Abstract

Tilt grain-boundary junctions with a 45° [001] misorientation were formed in $YBa_2Cu_3O_{7-x}$ (YBCO) thin films grown by pulsed organometallic beam epitaxy on (100) MgO substrates. The junctions were introduced at predetermined locations due to a modification of the orientation relation between the thin film and substrate following a low-energy argon ion irradiation of specific areas of the substrate surface prior to film deposition. Rutherford backscatter spectrometry and certain surface features observed by atomic force microscopy indicate that implantation of ions is necessary to cause the modified epitaxy. The low-temperature transport characteristics of individual isolated grain boundaries were determined by electromagnetic characterizations of the junction behavior. The same grain boundaries were examined by transmission electron microscopy and high-resolution electron microscopy and it was found that the boundaries are for the most part free of precipitates and well structured at the atomic scale. Regardless of the average grain boundary inclination, asymmetric (110)(100) facets dominate the microstructure of the junctions. Possible mechanisms for epitaxy modification and the transport properties in relation to the observed microstructure are discussed.

Keywords: Grain boundaries; Critical current density; Electrical resistivity; HREM; Thin films

1. Introduction

The Josephson-like properties of most high-angle grain boundaries in high-T_c materials have stimulated significant efforts in understanding and developing methods for producing such junctions. Grain boundaries have been introduced in a controlled manner by exploiting the ability to form high-quality epitaxial $YBa_2Cu_3O_{7-x}$ (YBCO) thin films on various substrates. These include bicrystal, bi-epitaxial and step-edge junctions, which all use the different possible epitaxial orientations of YBCO to the substrate to form grain boundaries.

Depending on the specific growth conditions YBCO thin films can grow with different epitaxial relations relative to (100) MgO [1–8]. The most

* Corresponding author. Fax: + 1 708 252 4798;
e-mail: karl_ merkle@qmgate.anl.gov.

common epitaxial orientation relationship observed is $YBa_2Cu_3O_{7-x}[001] \| MgO[001]$ and $YBa_2Cu_3O_{7-x}[110] \| MgO[110]$, otherwise referred to as cube-on-cube or 0° orientation. Another type of orientation relation often seen is $YBa_2Cu_3O_{7-x}[001] \| MgO[001]$ and $YBa_2Cu_3O_{7-x}[100] \| MgO[110]$ where the YBCO unit cell is rotated 45° about [001] relative to the cube-on-cube growth mode. This second type of orientation will be referred to as modified epitaxy or the 45° orientation, throughout the text. Previous work has suggested that under suitable conditions, ion beam modification of the substrate could induce a modified epitaxy [8]; however, this result could not be reproduced after the deposition chamber had been modified, probably due to changes in the growth conditions [9].

In this work a pre-growth sputter treatment of low-voltage argon ions was used to modify the epitaxial relation between the YBCO thin film and the MgO substrate. Under suitable deposition conditions YBCO thin films were grown on unmodified epitaxially polished (100) MgO substrates with cube-on-cube orientation. YBCO thin films grown on (100) MgO that had been irradiated with a low-energy Ar beam at normal incidence to the substrate grew with $YBa_2Cu_3O_{7-x}[001] \| MgO[001]$ and $YBa_2Cu_3O_{7-x}[100] \| MgO[110]$. By selective masking of the substrate prior to Ar irradiation, 45° [001] tilt grain boundaries were formed in the YBCO thin film. In the following we refer to such grain boundaries as sputter-induced grain boundaries or sputter-induced junctions.

The YBCO films were grown by pulsed metallorganic beam epitaxy (POMBE). This technique allows atomic layer by atomic layer deposition. Details of the deposition conditions used for YBCO film growth are described elsewhere [10,11]. It is well known that both the in-plane and out-of-plane epitaxial orientation of complex oxides can be controlled by deposition temperature [12], oxygen partial pressure [13], deposition rate [14], and in the case of atomic layer growth, the cation deposition sequence [15]. In this paper we will not address the highly complex issues connected with the precise control of the layer-by-layer deposition and its effect on epitaxy. However, we mention that recent refinements of the POMBE technique have allowed the growth of 45° rotated YBCO films on polished MgO (001) substrates and

0° oriented films in the Ar irradiated substrates. The application of this to the study of sputter-induced grain-boundary junctions will be the subject of a forthcoming publication [16].

The transport properties of YBCO grain boundaries have been studied extensively (see e.g. Ref. [17] for a review). Likewise there has been a considerable amount of work on the microstructure of YBCO grain boundaries (see e.g. Refs. [18–22]). However, direct connections between the microstructure and the transport properties are rarely made. In the present paper we investigate the formation, transport properties and microstructure of sputter-induced grain boundaries.

The main issues that we address are:

(1) What are the conditions and mechanisms for inducing the modified epitaxy of YBCO on (001) MgO?

(2) What are the transport properties of sputter-induced grain boundaries?

(3) What is their microstructure at length scales from the junction width down to the atomic scale?

(4) What insights into the weak-link nature of grain-boundary junctions can be gathered from comparing microstructure and transport properties?

2. Experimental procedure

Polished epitaxial quality (100) MgO single crystals from Coatings and Crystal Technology were treated in the following manner to generate 45° grain boundaries and study the conditions for modified epitaxy. To control the placement of the grain boundaries in the film the substrates were covered with either a metal shadow mask or Shipley 1218 photoresist prior to irradiation. The photoresist was found to provide a much sharper mask edge than the metal mask and was therefore used for most of the samples discussed. Standard photolithographic processes were used to define regions of the substrate to be irradiated. The sample was then ion irradiated using argon ions from a low voltage 3 cm diameter (50–1000 eV) Kaufman-type ion source for various incident ion angles, energies and durations as specified below. The substrate was mounted in good thermal contact to a copper stage and irradiated at room temperature. A standard condition for inducing

modified epitaxy was adopted: 250 eV ions at a 90° incidence (normal to the substrate surface) for 3 min with a beam current density of approximately 1 mA/cm^2. The photoresist was then removed using acetone and methanol. A YBCO thin film, typically between 2100 Å and 3000 Å thick, was deposited using pulsed organo-metallic beam epitaxy (POMBE) described in detail elsewhere [10]. It is important to note that the substrates were maintained in an oxygen plasma at growth temperature for at least 30 min prior to deposition. The growth temperature was typically in the range of 650–720°C and growth rates were 4–11 Å/min. The oxygen plasma was maintained during deposition and thus insured that the films were fully oxygenated.

The orientation of the films was determined by backscatter electron Kikuchi pattern analysis in a JEOL 6400 scanning electron microscope (SEM) (see for example Refs. [23] and [24]). The SEM was also used to study the film-surface morphology. Individual grain boundaries were subsequently isolated for transport measurements on a 40 μm wide microbridge. The microbridge was formed by 500 eV argon ion sputtering using a molybdenum mask and a liquid nitrogen cooled sample stage. The mask configuration allowed standard four-probe measurements of the grain boundary as well as the adjacent grains. Following the microbridge formation, the YBCO contact pads were sputter-cleaned with a low-energy ion beam and then silver contacts were evaporated in situ. The samples were subsequently annealed at 430°C for 5 h in flowing ultrahigh purity oxygen. Gold leads were connected to the sample using silver paint. The low-temperature measurements were performed in a cold finger helium flow cryostat that was shielded by Mu-metal. The Mu-metal shield was removed for transport measurements that were conducted in low magnetic fields both parallel and perpendicular to the sample in the range 0 to 200 G (0.01 G resolution). A 1 μV criterion was used in determining the critical current from the current–voltage (I–V) measurements.

Standard transmission electron microscopy (TEM) sample-preparation techniques were used to make plan view samples. The method involved grinding, dimpling and ion milling the sample to perforation. Special care was used to avoid exposure to water and high temperatures in order to minimize contamina-

tion and damage to the sample. Microstructural analysis was performed using a Phillips CM30 TEM at 100 kV. High-resolution electron microscopy (HREM) of the grain boundaries was done on a JEOL 4000 EXII, operated at 200 kV to minimize beam damage. Multislice calculations were performed using the NUMIS software package.

3. Results

3.1. Modified epitaxy

As described above, substrates were ion irradiated after specific areas had been masked. Subsequently, POMBE was used to deposit simultaneously a YBCO thin film across both the irradiated and unirradiated regions. The resulting orientation relation was $YBa_2Cu_3O_{7-x}[001] \parallel MgO[001]$ and $YBa_2Cu_3O_{7-x}[110] \parallel MgO[110]$ on the unsputtered region and $YBa_2Cu_3O_{7-x}[001] \parallel MgO[001]$ and $YBa_2Cu_3O_{7-x}[100] \parallel MgO[110]$ on the pre-sputtered region, forming a grain boundary at the common border of the two regions.

A variety of pre-growth irradiation conditions were used to determine the effect of the ions on the substrate and to map out a parameter space for which the modified epitaxy could be obtained. Backscattered electron Kikuchi patterns were used to determine the orientation of the film relative to the substrate. The orientation relation was correlated to the irradiation conditions to determine which conditions produced the modified epitaxy. Separately a series of substrates was prepared to study the effect of the various irradiation conditions on the substrate by Rutherford backscattering spectroscopy (RBS) and atomic force microscopy (AFM), which are used to analyze ion implantation and substrate surface topology respectively.

The incident ion angle relative to the substrate, the incident ion energy and the duration of irradiation were varied to determine the effect of these conditions on the YBCO epitaxy. Summarizing the results, as a function of the incident ion angle, the modified epitaxy occurred for angles greater than 45° (from the substrate surface). At incident angles of 45° and below only the cube-on-cube orientation was observed. With respect to the ion energy the epitaxy

was modified for energies from 500 eV down to 100 eV, but for 50 eV for an irradiation of 3 min at approximately 1 mA/cm^2 the epitaxy modification was not complete across the entire irradiated region. Therefore, it appears that there is a threshold energy for epitaxy modification between 50 eV and 100 eV. As for the duration of the sputter treatment, at 250 eV and 1 mA/cm^2 a minimum of 2 min was required to obtain the modified epitaxy.

RBS was used to determine the type, amount and location of implanted ions in the substrate due to irradiation. Under standard conditions (250 eV, 90° incidence for 3 min at 1 mA/cm^2) the RBS spectrum (see Fig. 2) had peaks for argon, as well as, surprisingly, for tungsten. The tungsten ions originate from the hot tungsten filament in the ion source. Analysis of the RBS spectrum indicates that within the resolution of the technique (4 nm) all the argon and tungsten is located at the substrate surface having a ratio of Ar:W = 10:1. The total number of argon ions embedded is approximately 9.52×10^{15} ions/cm^2 or approximately 1% of the irradiation dose. A TRIM code calculation [25], which is based on random binary collisions (i.e. it does not account for channeling and other crystalline effects), of low-voltage argon and tungsten bombarding a MgO substrate also indicates that under these conditions the ions would be expected to reside within the top 20 Å of the surface with the tungsten slightly deeper than the argon.

As the incident angle is varied from 90°, there is a marked decrease in the ion implantation (see Fig. 3). In a non-channeling condition at 45° incidence the amount of implanted Ar and W is 10% or less of the amount at 90° incidence. At 30° incidence no implanted Ar and W was detected in the substrate. Since no epitaxy modification was found for angles less than 45°, this suggests that the implanted ions are critical in causing the modified epitaxy. Therefore it appears that the latter is not solely caused by the irradiation-induced surface topology change.

The duration of the irradiation necessary to obtain modified epitaxy indicates that the W could play an important role in the surface modification. Fig. 4 shows that the amount of argon in the substrate saturates after 30 s of irradiation. The tungsten, however, continues to increase in a roughly linear manner up to 10 min (the maximum time measured).

The fact that the modified epitaxy occurs for sputtering times of greater than 2 min indicates that the tungsten could play a key role in causing the modified epitaxy. RBS measurements taken before and after the oxygen plasma anneal showed a noticeable reduction of the Ar and W RBS peaks. The reduction in the amount of Ar present after the anneal was somewhat larger for Ar, amounting to approximately 40% Ar and 70% W remaining for two samples measured, whereas only one sample showed a reduction to as low as 14% Ar and 42% W. Therefore we conclude that a significant fraction of the implanted Ar and W remained in the substrate even after an oxygen plasma anneal at the growth temperature.

In order to better understand the surface damage due to the ions, the MgO substrates were analyzed using AFM. Due to its hygroscopic nature the MgO surface is typically contaminated with hydroxides.
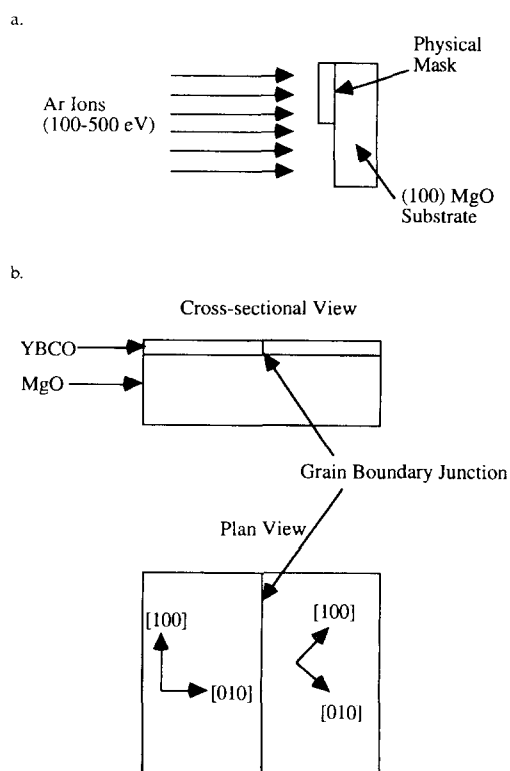

Fig. 1. Schematic of the sputter-induced epitaxy modification procedure for YBCO deposition onto (100) MgO. (a) Low-energy ion irradiation, normal incidence. (b) Grain-boundary junction geometry after YBCO thin film deposition by POMBE.
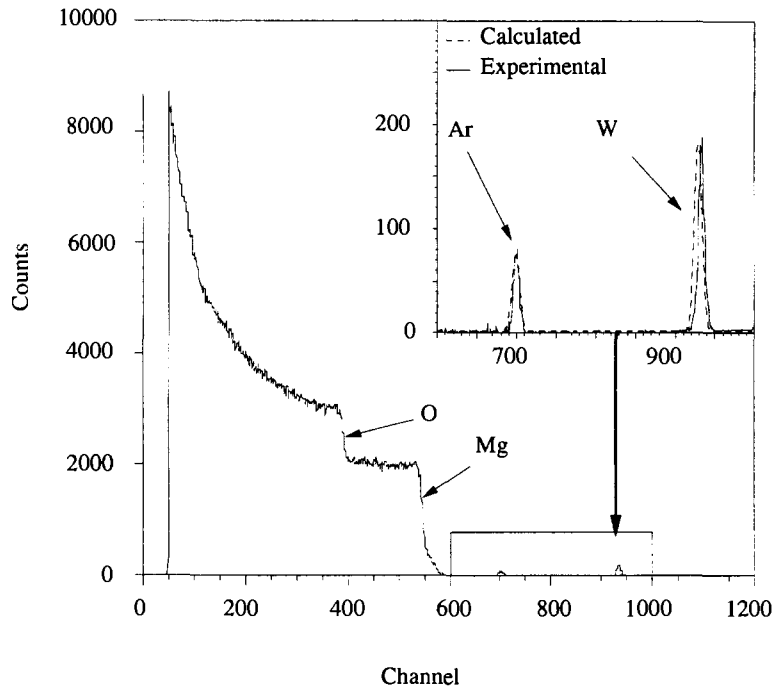
Fig. 2. Rutherford backscattering 1.6 MeV He analysis of MgO substrate. RBS spectrum of a (100) MgO substrate irradiated with argon ions at normal incidence for 3 min at 250 eV. The inset shows the backscattered intensities from the implanted Ar and W and the corresponding simulated spectra used in determining the amount of implanted species.
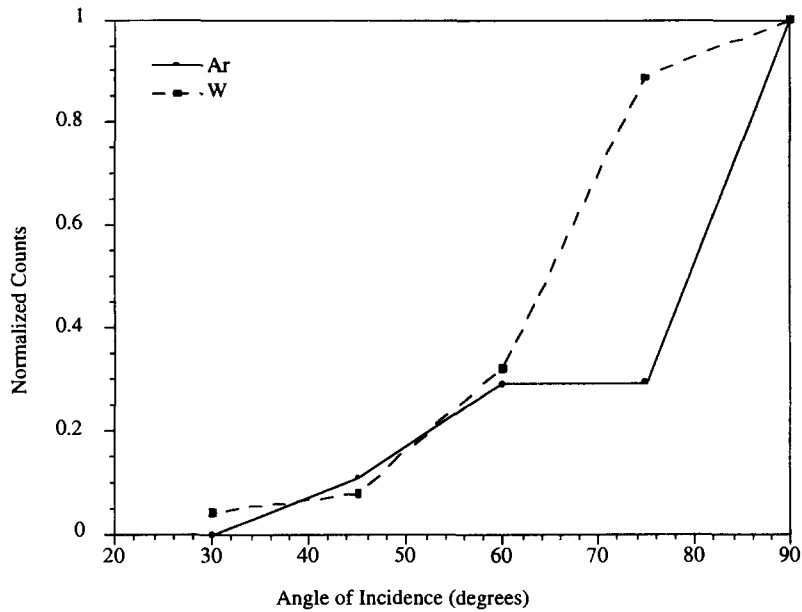

Fig. 3. Angular dependence of implanted argon and tungsten (relative amounts, normal incidence = 90°).
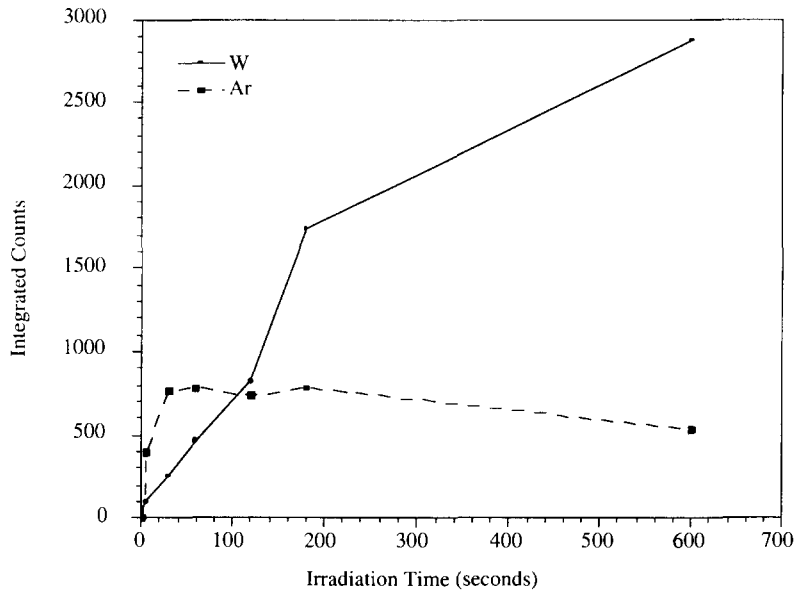
Fig. 4. Integrated counts in the He$^+$ backscattering peaks of argon and tungsten as a function of irradiation time. Note that the Ar implantation level reaches saturation early on in the irradiation.

Therefore to best imitate the growth surface of the substrate at the time of deposition, the samples were heated to the growth temperature and held in an oxygenated plasma for 30 min immediately prior to the ex-situ AFM analysis. This procedure was effective in removing contaminants from the substrate surface. Fig. 5 is an AFM image from an unsputtered region of the substrate. The substrate is relatively smooth on this length scale, with occasional damaged regions due to the chemical and mechanical polishes used to obtain the epitaxial quality finish. Fig. 6 is an AFM image from a sputtered region of
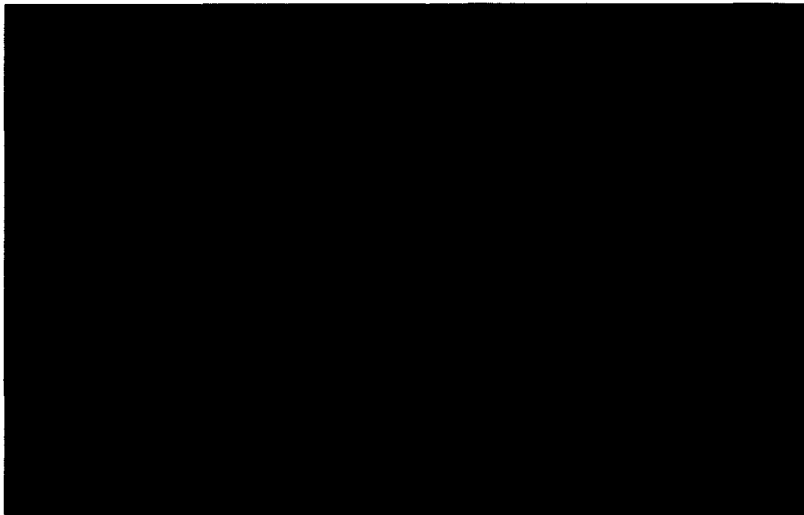

Fig. 5. Atomic force microscope image of a plasma annealed, but unirradiated (100) MgO substrate surface. Note relatively smooth surface topology.
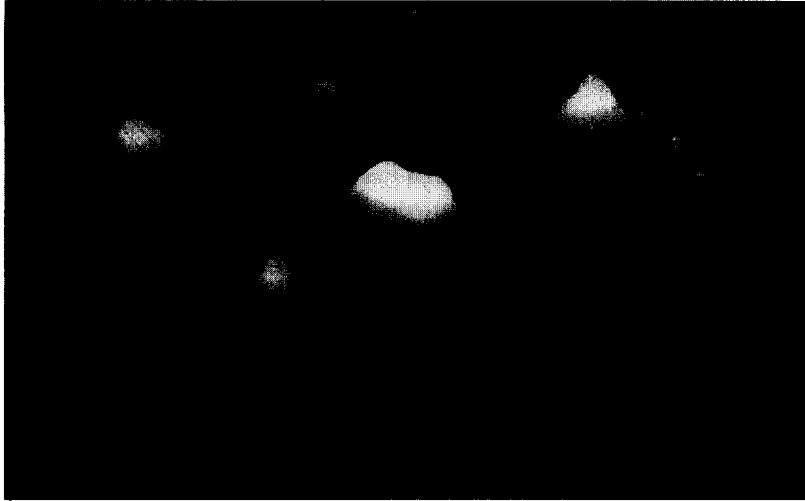
Fig. 6. Atomic force microscope image of a plasma annealed pre-irradiated (100) MgO substrate surface. The irradiation conditions were 250 eV argon ions for 3 min at normal incidence.

the substrate. Clearly the substrate surface is damaged after the sputtering. There are small mounds on the surface varying in size from 25 to 100 nm at the base and 5 to 10 nm in height. The possible origins of the mounds will be discussed below.

3.2. Transport properties

The low-temperature electrical transport properties of individual grain-boundary junctions were determined by a four-probe DC technique and included
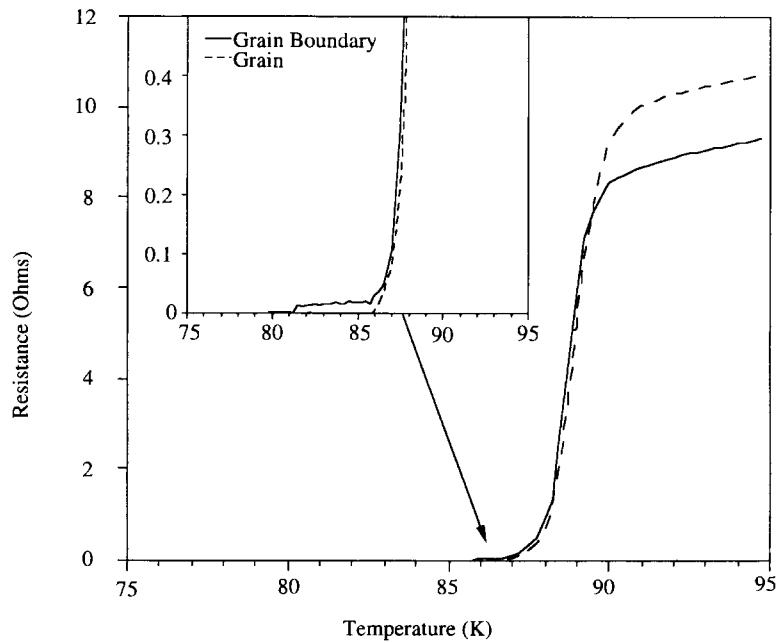

Fig. 7. Resistance vs. temperature characteristics of YBCO film for grain and grain boundary junction of 40 μm width. The inset shows a finite resistance in the grain-boundary foot structure.
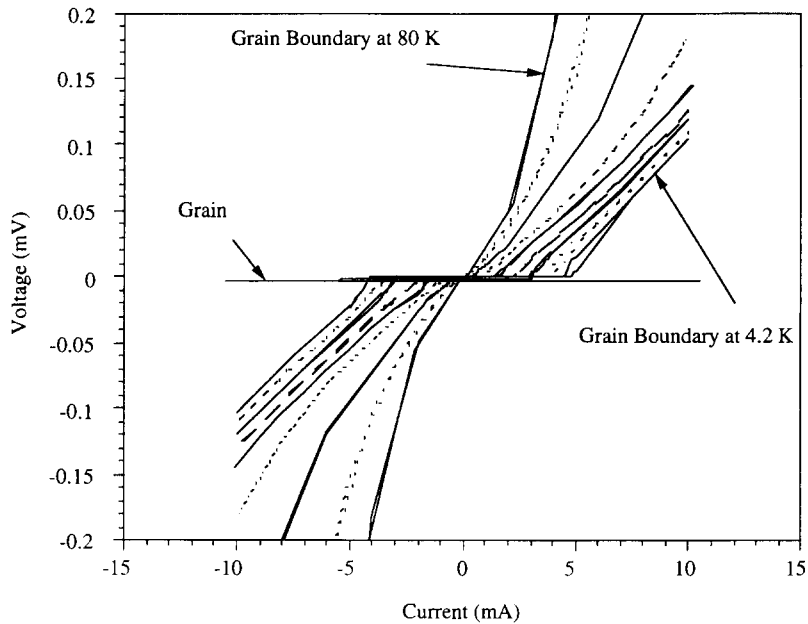
Fig. 8. *I–V* characteristics measured by DC four point probe technique for a 40 μm wide 45° grain boundary junction at 4.2 K, 20 K, 30 K, 40 K, 50 K, 60 K, 70 K, 77 K, and 80 K showing the transition from RSJ type behavior to flux-flow behavior.

measurements of the resistance-temperature (*R–T*), current–voltage (*I–V*) and low magnetic field dependences of the critical currents. Typical *R–T* char-

acteristics are shown in Fig. 7. Both the grains and grain boundary exhibit an abrupt decrease in resistance at approximately 86 K. The measurement across
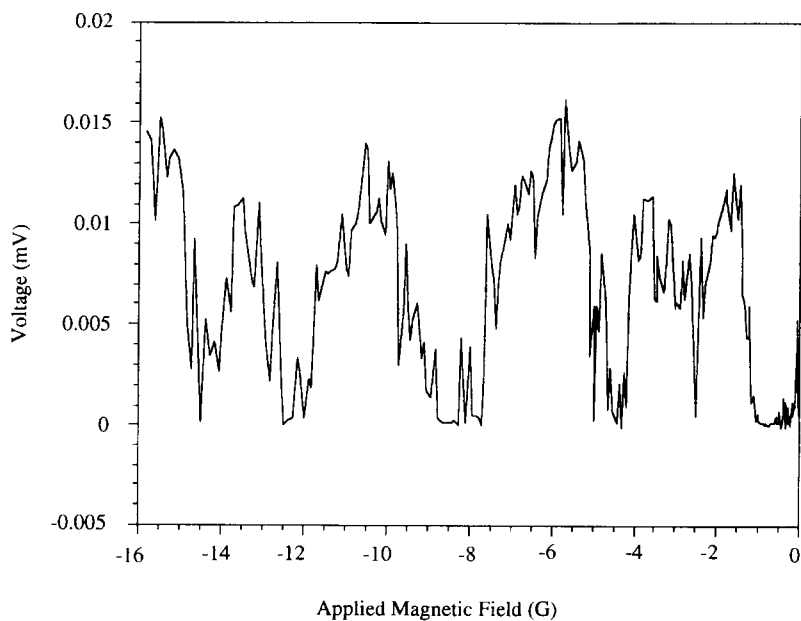

Fig. 9. Voltage vs. applied magnetic field on a DC current biased grain-boundary junction of 40 μm width at 4.2 K. Note fluctuations at different frequencies. The variations reflect the critical current behavior as a function of magnetic field.

the grain boundary includes the normal-state resistance of the grains surrounding the boundary as well as the grain boundary. Therefore, when the two grains are superconducting the resistance measured is fully attributable to the boundary. In Fig. 7 the grain goes fully superconducting at 86 K, but the grain boundary maintains a finite resistance. The boundary resistance decreases slightly until it abruptly goes superconducting at 81.25 K. This extended foot-like structure in the grain-boundary resistance is due to the weak-link behavior, i.e. the reduced critical current $I_c(T)$ across the boundary. The Josephson coupling energy ($E_J = \Phi_0 I_C(T)/2\pi$, where Φ_0 is the flux quantum), which is reduced across the grain boundary, becomes comparable to the thermal energy ($E_T = k_B T$), close to the transition temperature. Thus, thermal fluctuations can cause noise and a finite resistance. Such effects have been observed in other Josephson junctions and have been discussed in the literature [17,26,27]. In some samples that were formed using a metal mask, a small transition region was formed that contained several grain boundaries across the junction. In this case no foot structure was observed, rather a broad-

Fig. 11. Asymmetric (110)(100) facets along a length of a sputter-induced epitaxy grain boundary. As the average grain-boundary plane changes its inclination near the top of the image strong asymmetric faceting is maintained.
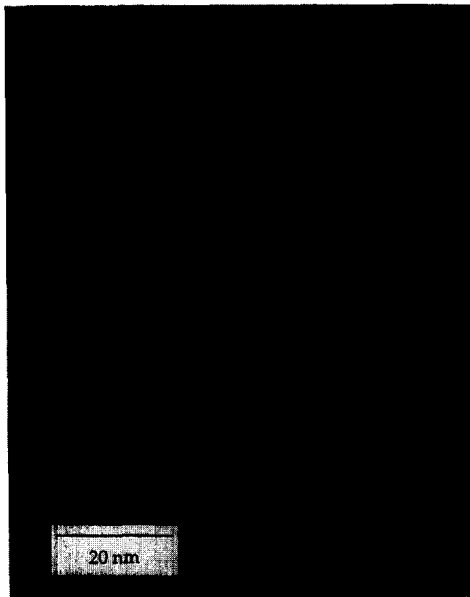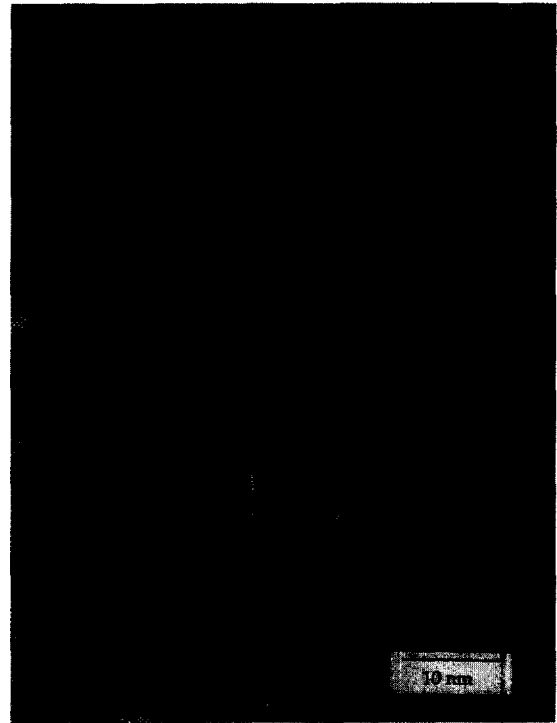

Fig. 10. A HREM micrograph of a 100 nm long asymmetric facet at the grain boundary. The (100) planes of the left grains are parallel to the (110) planes of the adjacent grain.

ening of the resistive transition was found. Therefore, the observation of a foot structure and a sharp grain-boundary transition also appears to be indicative of single grain-boundary junction behavior.

The $I–V$ characteristics of a sputter-induced epitaxy grain boundary at temperatures between 4 and 80 K is shown in Fig. 8. The grains remain superconducting throughout this temperature range, but the grain boundary has typical weak-link behavior becoming manifest at a reduced critical current density. At 4.2 K the critical current density of this grain boundary is 5.1×10^4 A/cm^2. The $I–V$ curve at low temperatures can be modeled as a resistively shunted junction (RSJ). As the temperature is increased the critical current density goes down to 1.6×10^3 A/cm^2 at 77 K. At the higher temperatures the shape of the curve changes from RSJ to flux-flow-type behavior. Also, at temperatures close to T_c the effect of thermal noise can be observed in the $I–V$ curves as a small finite resistance at low currents.
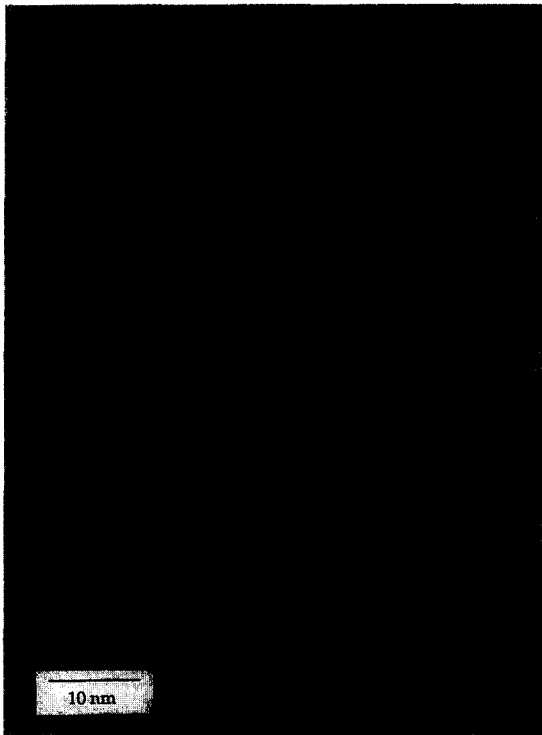
Fig. 12. HREM image of a grain-boundary region in which the grain boundary changes it inclination by more than 90°, but maintains asymmetric facets along the entire length. The region indicated by the arrow is magnified in Fig. 13.

The variation of the voltage across the boundary as a function of applied magnetic field for a junction crosssection of approximately 10 μm^2 is indicated in Fig. 9. The magnetic field was applied perpendicular to the film surface and parallel to the grain boundary. The sample was biased with a constant current just below the maximum critical current while the voltage across the grain boundary was monitored as the magnetic field was varied. This voltage is inversely related to the critical current across the boundary and thus can serve as an indication for the variations in critical current as a function of magnetic field. In Fig. 9 relatively high frequency oscillations (on the order of 0.05 G) as well as a longer periodicity of about 4 G can be distinguished. Two important features of the resulting magnetic field behavior are

(1) the critical current never goes to zero suggesting non uniform current distribution along the boundary,

and (2) the magnetic field behavior suggests a rather inhomogeneous transport across the GB.

A perfect Fraunhofer interference pattern is expected for a Josephson junction with a uniform current distribution distribution along its length. A more detailed description and analysis of the magnetic-field behavior and comparison to other samples with identical misorientations will be provided elsewhere [28].

3.3. Microstructure

Scanning electron microscopy was used for the initial analysis of the film surface and the grain boundary. The film-surface structure varied with the specific growth conditions but was uniform across the entire substrate for each run. This is in contrast to
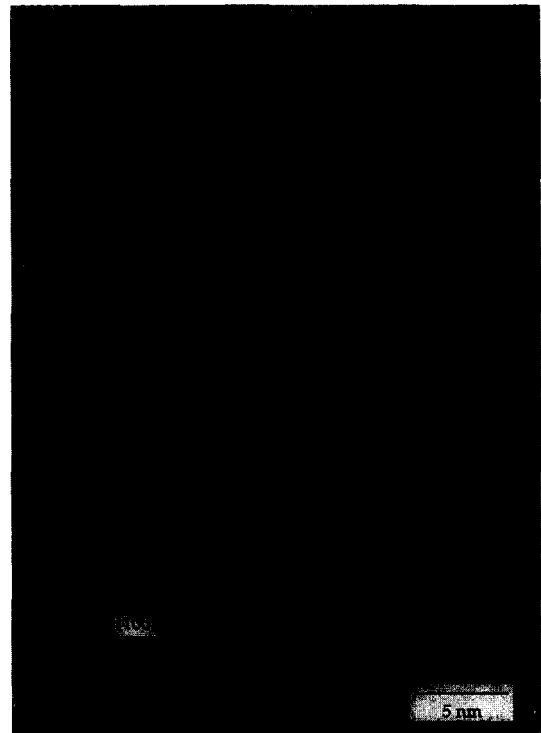

Fig. 13. Microfacetted region of the grain boundary in Fig. 12. The boundary is stepped with asymmetric (110)(100) microfacets maintaining the local asymmetry. The "step" regions have reversed symmetry, i.e. (100)(110) in the "ledge" regions. Thus, the same asymmetric grain-boundary geometry is maintained over the entire length.

observations on bi-epitaxial thin YBCO films, where the chemical nature of the substrate is different across the 45° boundary, causing a different surface morphology among the grains. In this case the position of the grain boundary can often easily be recognized, for example, due to a different density of surface precipitates. Moreover, such chemical effects can also give rise to different transition temperatures in the adjoining grains [29,30]. The uniform structure of the films in the present work on both the sputtered and unsputtered sides meant that the location of the grain boundary could typically only be identified by backscattered electron Kikuchi pattern analysis. The grain boundary appeared straight within the resolution of the SEM and the Kikuchi patterns of about 1 micron. SEM images of the sputter-induced grain boundaries are published elsewhere [11,23,24].

Transmission electron microscopy was used for more detailed analysis of the grain-boundary struc-

Fig. 15. Rigid atomic model of the (110)(100) grain boundary used for the image simulation inset in Fig. 16. Shown are the atomic configurations for three layers in the $a-b$ plane: (a) the CuO chain layer, (b) the CuO_2 square layer and (c) the BaO layer. A grain-boundary supercell equivalent in size to 10×10 YBCO unit cells was used.
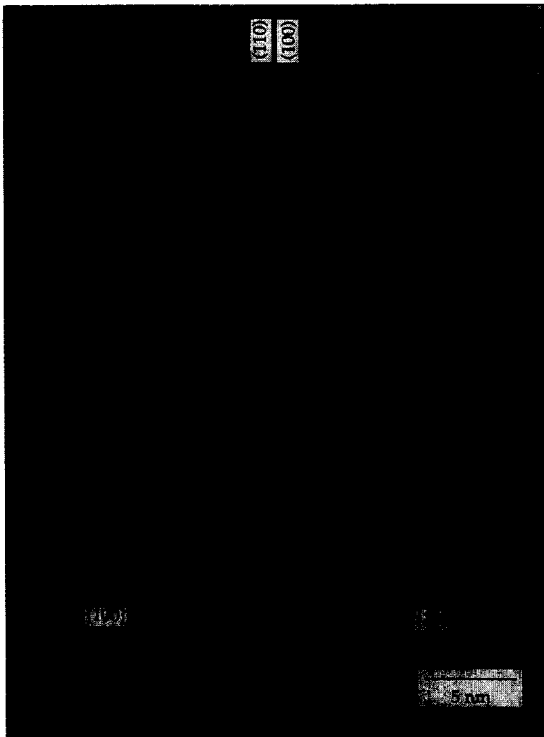

Fig. 14. HREM image of a 40 nm long asymmetric facet along a grain boundary. The boundary maintains the grain structure to within one interplanar spacing on both sides of the interface.
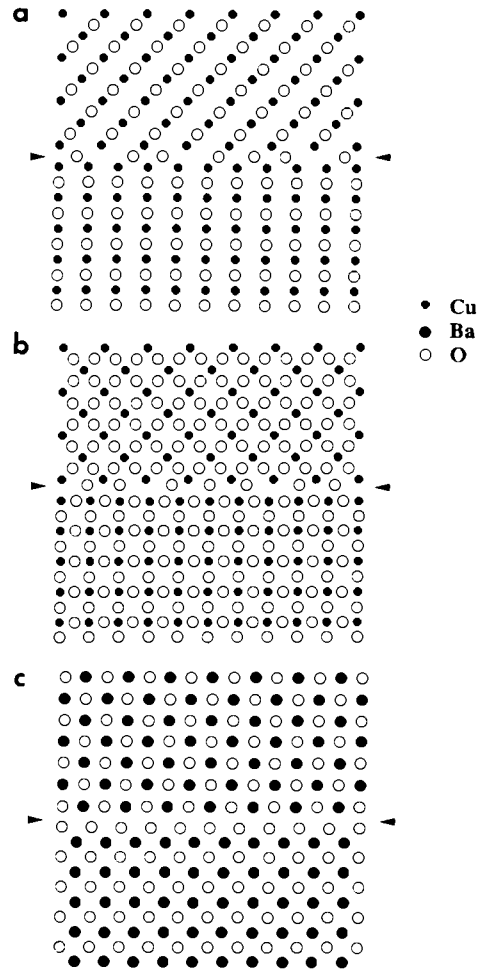
ture. It was found that the boundary does not traverse the substrate length absolutely straight; rather it meanders about the border between the sputtered and unsputtered MgO. The excursions of the boundary from a hypothetical straight line are on the order of 200 nm. This type of meandering is seen on different length scales in all YBCO thin-film grain boundaries and is dependent on several variables [21,22]. First, the photolithographic patterning process cannot pro-

duce a perfectly straight line. Therefore, the border of the sputtered region will not be perfectly straight. Secondly, the higher growth rate in the a–b direction than in the c direction allows for interpenetration of the grain across the substrate template. This is well documented in bicrystal cases where penetration of grains across the substrate boundary has been found [22]. In the bicrystal the grain that penetrates across the templated substrate defies the highly preferred orientation due to the accelerated a–b growth. A major implication of this type of thin-film growth is that the microscopic grain-boundary geometry can vary substantially from the macroscopic one.

The boundaries were only occasionally disrupted by precipitates. There was no preferential segregation of precipitates to the boundary as is seen in some other types of junctions [28]. Typically less than 5% of the boundary was disrupted by precipitates.

An important feature of the sputter-induced epitaxy grain boundaries is the special faceting along their length. Over approximately 70% of the total boundary length the same type of asymmetric facet was observed. These facets had (100) planes of one grain parallel to (110) planes of the adjacent grain.

This low-index plane asymmetry existed in regions as long as 100 nm without disruption (see Fig. 10). Even as the average boundary plane rotated into a different inclination, the (110)(100) asymmetry was maintained (see Fig. 11). The amount of faceting observed for these films, grown close to thermodynamic equilibrium conditions, suggests that these asymmetric grain boundaries represent a low-energy configuration. Since these facets are the predominant microstructural feature of the grain boundary they would be expected to also dominate the transport properties.

An image of a grain boundary that changes its inclination by more than 90° in the (001) plane is shown in Fig. 12. Along the entire length of this image the boundary maintains the low-index plane asymmetry described above. The longer facets clearly display this asymmetry and in closer analysis so do the steps connecting the microfacets (see Fig. 13). In this microfaceted region the "ledges" show the (100) of the left grain parallel to the (110) of the right grain. As the boundary "steps" the asymmetry is reversed, but maintains the same low-index planes with the (110) of the left grain parallel to the (100) of the right grain. This type of extensive faceting

Fig. 16. An HREM image and image simulation of a (110)(100) grain boundary based on the model structure of Fig. 15. The simulation is at −40 nm defocus and a sample thickness of 11.4 nm.

was not observed for other grain boundaries with the same macroscopic geometry, but prepared by bi-epitaxy, using laser ablation [28]. Both the longer and shorter facets show very little distortion of the adjacent grains up to the boundary. Figs. 13 and 14 suggest that there is an insignificant amount of strain in the lattice outside of a region within a couple of interplanar spacings of the grain boundary. A multi-slice simulation of the grain boundary confirms this by using a rigid model whose unit cells are only modified within a total of 4 Å (i.e. ±2 Å) of the grain-boundary plane (see Fig. 15). The model used was a rigid model cut off at the (100) plane of one grain parallel to the (110) plane of the adjacent grain. For the CuO chain and CuO$_2$ square layers the boundary shares a common oxygen layer of both grains on each side. However, for the BaO layer the terminating planes at the boundary are BaO and O planes for both grains, respectively. Y has the same position as Ba in the a–b plane and therefore is not shown in Fig. 15. The grain-boundary region between the two planes was modified by adjusting the interplanar spacing at the grain boundary and by removing several oxygen atoms at the boundary core. The simulation does not match the entire grain-boundary image due to the aperiodicity of the grain-boundary structure; however, there are features that can be qualitatively compared. The model reproduces the streaking and heightened intensity observed along some regions of the boundary. This reflects the highly localized disordered region at the boundary.

4. Discussion

Attempts to modify the thin-film epitaxial orientation via the sputtering of a substrate prior to deposition have seldom been successful and the sputtering procedures reported here, in conjunction with precise control of the POMBE deposition conditions appear to be the only method, up to now, to reproducibly obtain sputter-induced epitaxy modification in YBCO thin films. Recently Buchholz et al. have performed detailed investigations of the POMBE deposition conditions that allow the deposition to occur of 45° rotated [001] YBCO films on unsputtered MgO and 0° oriented films on sputtered MgO; this will be

reported elsewhere [16]. To understand the reasons for creating the second favorable orientation for the YBCO on MgO we examine the structural relationship between the two materials. Initial studies of YBCO on MgO generally produced polycrystalline films with the 45° orientation appearing to be the second most observed after the 0° (cube-on-cube) [2–4]. The mismatch between YBCO and MgO, as calculated by the near-coincidence site lattice theory, is relatively large (8.89%) in the cube-on-cube orientation and significantly smaller (2.29%) for the 45° orientation [31]. The preference of the 0° orientation by the nucleation at steps that fixes the geometry in two mutually perpendicular directions has been suggested by Ravi et al. [3] It has also been suggested that the cube-on-cube orientation dominates despite a larger lattice mismatch because it has the best coordination between the YBCO and MgO oxygen sub-lattices [1]. Although geometrical models have been applied, the origin of the 45° rotated grains which have been frequently observed under a variety of deposition conditions remains somewhat elusive. The driving forces for the two orientations are significantly different; however, both appear to be configurations of relatively low energy. The 0° orientation seems to dominate when there are many ledge sites and the 45° orientation appears to be favored in the absence of ledge sites due to the smaller lattice mismatch between the film and substrate. Furthermore, the precise deposition conditions can also dictate the orientation of the film by varying the kinetic and structural parameters during deposition.

The combination of the RBS and AFM examination of the MgO substrate provides insight into the mechanisms causing the modified epitaxy of the YBCO thin film. The AFM images provide evidence that there is a significant change in surface morphology after irradiation. The RBS data suggest that ion implantation is also necessary to induce the modified epitaxy. At the lower irradiation angles where only the surface morphology would be changed and practically no implantation occurs, the modified epitaxy is not observed.

As potential causes for the modified epitaxy we consider four basic substrate-surface effects. First there can be localized surface-lattice strains due to the ion implantation. The YBCO is in a state of tensile strain in the cube-on-cube orientation; how-

ever, studies of ultrathin films of YBCO on MgO have shown that the a-axis lattice parameter of the 45° orientation is compressed [32]. Both implanted argon and tungsten could produce localized expansion of the lattice. Any distortion that increases the MgO lattice parameter would increase the misfit for the cube-on-cube orientation. However, the 45° orientation would become more favorable because of a smaller misfit. Therefore, one possibility is that a locally altered lattice parameter due to the implanted ions favors the second orientation. Two possible ways to modify the local lattice parameter are discussed here. First, tungsten could be important due to the fact that the amount of argon saturates in the substrate after 30 s of irradiation, whereas the tungsten deposition continues to increase linearly with time. Therefore, since the modified epitaxy only occurs for times greater than 2 min, the tungsten may be necessary in the process. The second possibility is that argon clusters in the form of small (submicroscopic) bubbles are present close to the surface. The absolute quantity of implanted argon is significantly greater than that of tungsten. The argon will have to form clusters since only those can be expected to be stable at the growth temperature. This could also account for the finite irradiation dose which is necessary for establishing the modified epitaxy effect. Moreover, ion channeling is probably necessary to deposit the Ar in subsurface clusters that are stable and resist escape to the surface. Each subsurface Ar bubble would have substantial internal pressure which would cause considerable lattice strain and a local expansion of the lattice parameter at the surface directly opposite the Ar cluster. Some of these clusters could possibly give rise to the bumps observed in the AFM images of the irradiated surface. Both arguments are consistent with the fact that the implanted ions are necessary for inducing the modified epitaxy.

The third effect on the substrate is the surface roughening which occurs due to the ion irradiation. The stepped structure of an MgO surface appears to favor the cube-on-cube orientation as mentioned previously. However, since at an ion incidence of 45° and lower the modified epitaxy was not observed surface damage alone cannot account for the observed effects. At the lower incident angles the step structure of the substrate would still be severely

modified and yet the epitaxy remains cube-on-cube. This strongly implies that the ion implantation plays an essential role, possibly being the major factor, in modifying the epitaxy. It should be noted that the reproducibility of this process is probably also associated with the use of an oxygen plasma in the growth chamber that provides a reproducible growth environment by removing any possible contamination layers from the substrate prior to deposition.

The fourth effect that needs to be considered is the possibility of modifying the surface chemistry and thus modifying the substrate–film interactions. It is unclear how and at what specific sites the implanted ions are located in the surface region. The specific location of the ions could play a role in changing the interfacial energy of the YBCO/MgO interface due to impurities. The W can have several different valences and could, for chemical reasons, be a favorable nucleation site. This possibility could be explored by using different ions and conditions and to study the surface using surface sensitive analytical techniques such as X-ray photoemission spectroscopy (XPS). We note that in contrast to argon, the tungsten could reside at the surface directly.

The necessity of using bulk MgO crystal substrates has been circumvented recently by reproducibly forming sputter-induced epitaxy grain boundaries on thin films of MgO deposited on LaAlO$_3$ [23]. The use of an in situ deposited MgO film indicates that there is no connection of this technique to the chemical and mechanical polishing (as a possible contamination source) involved in the commercial preparation of the bulk MgO. The major implication is that this technique can be translated to other more favorable bulk substrates for integration by deposition of a high quality epitaxial MgO layer.

The transport properties of these grain-boundary junctions are particularly good considering the high misorientation angle between the grains. Although higher critical current densities have been reported for polycrystalline films grown on MgO [3,33], the critical current densities for the present samples are higher than any reported for the same 45° [001] misorientation angle of both bi-epitaxial and bicrystal boundaries [17,34–37]. The sputter-induced epitaxy junctions even maintain higher critical current densities than some lower-angle junctions reported

[37]. A comparison of the structure to the transport properties provides significant insight into their microstructural origin.

Two implications about the supercurrent transport follow from the transport properties of these junctions. First, the higher critical current densities compared to other junctions with the same misorientations indicate that there is more supercurrent traversing the boundary than with other grain boundaries of the same macroscopic misorientation (see for example Ref. [30]). This could be the result of undisrupted grain boundary regions, i.e. fewer second phases or precipitates. Alternatively the favored low-index plane facets may be able to maintain a higher critical current density than other grain-boundary facets. The second implication of the transport properties can be derived from the magnetic-field data. Comparing the latter to 45° [001] tilt bi-epitaxial junctions, the critical current versus magnetic field dependence shows a significantly higher fraction of long period fluctuations in the junctions produced by sputter-induced epitaxy. This suggests that there is a more uniform current distribution along the boundary length, which is also implicit in the quite uniform grain-boundary geometry, i.e. the predominance of (110)(100) facets. The asymmetric facets, which are not as predominant and well structured in the bi-epitaxial junctions, may also support higher current densities (a more detailed comparison with other types of grain boundaries is made elsewhere [38]).

As discussed above, the (100)(110) asymmetric facets are the dominant microstructural feature of these grain boundaries. Therefore, the grain boundary consists of basically one type of grain boundary. HREM observations show that the facets appear to be well structured up to the grain boundary. It has been suggested in the literature that grain boundaries that combine low-index planes have low energy and it was also shown that asymmetric grain boundaries can have lower energy than the corresponding symmetric boundaries [39]. The (110)(100) facets formed regardless of the macroscopic symmetry of the grain boundary. Thus, although the meandering implied the presence of a multitude of grain-boundary inclinations it is clear that the microscopic geometry cannot be derived from the macroscopic one. It also appears that due to the short coherence length, the microscopic structure and symmetry will dominate

the transport properties. Potentially larger current densities across the asymmetric facets have also been suggested by a theoretical calculation based on dislocation strain of symmetric and asymmetric grain boundaries [40].

The atomic-scale structure of the [001] 45° asymmetric grain boundary suggests a basis for their weak-link nature. Despite of the well-structured grains up to the grain-boundary plane, HREM image simulations based on model structures, such as in Fig. 15, indicate that there must be a region of structural and chemical disorder, approximately 4 Å wide at the boundary. This type of disorder must involve oxygen-defect sites that are essentially localized at the grain-boundary plane. Therefore, even in these well structured grain boundaries a significant quantity of defect sites exist which can give rise to the weak-link behavior. It is well known that oxygen depletion near boundaries strongly affects electrical transport properties. Moreover, local lattice strains can give rise to local oxygen deficiencies. Although the HREM technique is not sensitive to the detection of oxygen, the absence of significant long-range strain fields in the vicinity of the boundary suggests that wide regions depleted of oxygen do not play a role in these boundaries. Nevertheless this needs to be investigated by EELS measurements. Browning et al. have used EELS to quantify the hole depletion at a symmetric and an asymmetric YBCO grain boundary and find no depletion and a 10 nm wide depletion region, respectively [18]. Local variations in the density of defects and oxygen depletion along the length of the boundary can produce regions of stronger and weaker coupling across the boundary. The challenge remains to identify the nature and the scale of the inhomogeneities along the grain boundary and directly relate these to the corresponding microstructural features.

In summary, sputter-induced epitaxy grain boundaries have been formed on (100) MgO substrates using a pre-growth sputter treatment. The cause for the modified epitaxy is most likely a combination of the surface disorder and the effect of ion implantation on the surface structure. The grain boundaries have good transport properties that must be directly related to the formation of low-index plane facets that have been observed along the majority of the boundary length.

Acknowledgements

References

[1] L.A. Tietz, C.B. Carter, D.K. Lathrop, S.E. Russek, R.A. Buhrman and J.R. Michael, J. Mat. Res. 4 (1989) 1072.

[2] S. McKernan, M.G. Norton and C.B. Carter, J. Mater. Res. 7 (1992) 1052.

[3] T.S. Ravi, D.M. Hwang, R. Ramesh, S.W. Chan, L. Nazar, C.Y. Chen, A. Inam and T. Venkatesan, Phys. Rev. B 42 (1990) 10141.

[4] R. Ramesh, D. Hwang, T.S. Ravi, A. Inam, J.B. Barner, I. Nazar, S.W. Chan, C.Y. Chen, B. Dutta, T. Venkatesan and X.D. Wu, Appl. Phys. Lett. 56 (1990) 2243.

[5] B.H. Moeckly, S.E. Russek, D.K. Lathrop, R.A. Buhrman, J. Li and J.W. Mayer, Appl. Phys. Lett. 57 (1990) 1687.

[6] M.G. Norton and C.B. Carter, J. Cryst. Growth 110 (1991) 641.

[7] S.-T. Lee, S. Chen, L.S. Hung and G. Braunstein, Appl. Phys. Lett. 55 (1989) 286.

[8] N.G. Chew, S.W. Goodyear, R.G. Humphreys, J.S. Satchell, J.A. Edwards and M.N. Keene, Appl. Phys. Lett. 60 (1992) 1516.

[9] N.G. Chew, private communication.

[10] D.B. Buchholz, S.J. Duray, D.L. Schulz, T.J. Marks, J.B. Ketterson and R.P.H. Chang, Mater. Chem. Phys. 36 (1994) 377.

[11] K.A. Dean, D.B. Buchholz, L.D. Marks, R.P.H. Chang, B.V. Vuchic, K.L. Merkle, D.B. Studebaker and T.J. Marks, J. Mater. Res. 10 (1995) 2700.

[12] D. Chambonnet, D. Keller, A. Gervais, C. Fayes, S. Degoy and C. Belovet, Physica C 235–240 (1994) 625.

[13] R. Feenstra, T.B. Lindermer, J.D. Budai and M.D. Gallaway, J. Appl. Phys. 69 (1991) 566.

[14] T. Burmann, J. Geerk, O. Meyer, R. Schneider and G. Linker, Solid State Commun. 90 (1994) 599.

[15] R.A. McKee, F.J. Walker, E.D. Specht, J.G.E. Jellison and L.A. Boatner, Phys. Rev. Lett. 72 (1994) 2741.

[16] D.B. Buchholz, J.S. Lei, S. Mahajan, P.R. Markworth, R.P.H. Chang, B. Hinds, T.J. Marks, J.L. Schindler, C.R. Kannewurf, Y. Huang and K.L. Merkle, to be published.

[17] R. Gross, in: Interfaces in Superconducting Systems, eds. S.L. Shinde and D. Rudman (Springer, New York, 1992) p. 1.

[18] N.D. Browning, M.F. Chisholm and S.J. Pennycook, Interface Sci. 1 (1993) 309.

[19] Y. Gao, K.L. Merkle, G. Bai, H.L.M. Chang and D.J. Lam, Physica C 174 (1991) 1.

[20] J.A. Alarco, E. Olsson, Z.G. Ivanov, P.A. Nilsson, D. Winkler, E.A. Stepantsov and A.Y. Tzalenchuk, Ultramicroscopy 51 (1993) 239.

[21] C. Traeholt, J.G. Wen, H.W. Zandbergen, Y. Shen and J.W.M. Hilgenkamp, Physica C 230 (1994) 425.

[22] D.J. Miller, T.A. Roberts, J.H. Kang, J. Talvacchio, D.B. Buchholz and R.P.H. Chang, Appl. Phys. Lett. 66 (1995) 2561.

[23] B.V. Vuchic, K.L. Merkle, K.A. Dean, D.B. Buchholz, R.P.H. Chang and L.D. Marks, Appl. Phys. Lett. 67 (1995) 1013.

[24] B.V. Vuchic, K.L. Merkle, K.A. Dean, D.B. Buchholz, R.P.H. Chang and L.D. Marks, J. Appl. Phys. 77 (1995) 2591.

[25] J. Biersack and L. Haggmark, Nucl. Instr. and Meth. 174 (1980) 257.

[26] V. Ambegaokar and B.I. Halperin, Phys. Rev. Lett. 22 (1969) 1364.

[27] R. Gross, P. Chaudhari, D. Dimos, A. Gupta and G. Koren, Phys. Rev. Lett. 64 (1990) 228.

[28] B.V. Vuchic, PhD. thesis, Northwestern University (1995).

[29] B.V. Vuchic, K.L. Merkle, K.A. Dean, D.B. Buchholz, R.P.H. Chang and L.D. Marks, in: MRS, eds. D. Bonnell, M. Rühle and U. Chowdhry 357 (1994) 419.

[30] B.V. Vuchic, K.L. Merkle, K. Char, D.B. Buchholz, R.P.H. Chang and L.D. Marks, J. Mater. Res. (1996), to be published.

[31] D.M. Hwang, T.S. Ravi, R. Ramesh, S.-W. Chan, C.Y. Chen, L. Nazar, X.D. Wu, A. Inam and T. Venkatesan, Appl. Phys. Lett. 57 (1990) 1690.

[32] S.K. Streiffer, B.M. Lairson, C.B. Eom, B.M. Clemens, J.C. Bravman and T.H. Geballe, Phys. Rev. B 43 (1991) 13007.

[33] D.K. Lathrop, B.H. Moeckly, S.E. Russek and R.A. Buhrman, Appl. Phys. Lett. 58 (1991) 1095.

[34] D. Dimos, P. Chaudhari and J. Mannhart, Phys. Rev. B 41 (1990) 4038.

[35] K. Char, M.S. Colclough, L.P. Lee and G. Zaharchuk, Appl. Phys. Lett. 59 (1991) 2177.

[36] E.A. Early, R.L. Steiner, A.F. Clark and K. Char, Phys. Rev. B 50 (1994) 9409.

[37] Z.G. Ivanov, P.Å. Nilsson, D. Winkler, J.A. Alarco, T. Claeson, E.A. Stepantsov and A.Y. Tzalenchuk, Appl. Phys. Lett. 59 (1991) 3030.

[38] B.V. Vuchic, L.D. Marks and K.L. Merkle, to be published.

[39] K.L. Merkle and D. Wolf, Philos. Mag. A 65 (1992) 513.

[40] E.Z. Meilikhov, Physica C 226 (1994) 69.